Int J Adv Manuf Technol (2015) 78:593–602
DOI 10.1007/s00170-014-6685-7

ORIGINAL ARTICLE

Numerical simulation of plasma arc welding with keyhole-dependent heat source and arc pressure distribution

T. Q. Li · C. S. Wu

Received: 23 June 2014 / Accepted: 1 December 2014 / Published online: 10 December 2014

Abstract A three-dimensional and transient model with keyhole geometry-dependent heat source and arc pressure distribution is developed for plasma arc welding process. The influence of the keyhole evolution on heat flux and arc pressure distribution on the keyhole wall is taken into consideration. The dynamic variation of the temperature field and fluid flow in the weld pool as well as the keyhole shape and size are quantitatively analyzed. The experimentally observed phenomena, i.e., the backward curved keyhole channel and the very thin layer of molten metal at the front edge of weld pool, are first demonstrated with numerical simulation. The predicted establishment time of open keyhole, displacement of keyhole exit, and fusion line generally agree with the experimental ones.

Keywords Plasma arc welding · Keyhole · Weld pool · Keyhole-dependent heat source · Keyhole-dependent arc pressure distribution

1 Introduction

Plasma arc welding (PAW) can fully penetrate stainless steel plates of 6–10 mm thickness with one single pass when it works at keyhole mode [1]. The plasma arc torch has a water-cooled copper nozzle in front of the cathode to constrict the arc plasma through thermal pinch effect, so that the arc plasma with high energy density and high arc pressure can be produced. As schematically shown in Fig. 1, when the plasma arc impinges on the area where two workpieces are to be joined, it can melt material and create a molten liquid pool (weld pool). Because of its high velocity and the associated momentum, the plasma arc can penetrate through the molten pool and form a keyhole in the weld pool. Moving the welding torch and the associated keyhole will cause the flow of the molten metal surrounding the keyhole to the rear region where it resolidifies to form a weld bead [2]. Compared to laser beam welding (LBW) and electron beam welding (EBW), which can produce large weld penetration under keyhole mode [3–5], PAW process is lower in cost, more tolerant of joint preparation, and easier in operation [3]. However, PAW process has one weakness, i.e., the process parameter window to get good quality weld is narrower [2, 6, 7]. To improve the practical adaptability of PAW process, it is essential to understand the mechanism of keyhole establishment and sustainment as well as the correlation of the process parameters with the keyhole dynamics.

Lots of attempts have been made to conduct numerical analysis of the fluid dynamics and temperature distributions in keyhole PAW weld pool. For simplification, some researchers did not consider the existence of keyhole and focused on the heat transfer and fluid flow phenomena in weld pool [8, 9], and others took prescribed keyhole shape in their models [10, 11]. Such treatment of keyhole differs much from the real case in keyhole PAW. To demonstrate the keyhole evolution, two-dimensional models for stationary keyhole PAW were developed [12–14]. In fact, keyhole PAW involves in three-dimensional fluid flow and heat transfer since the welding torch is moving. Recently, Wu's group developed three-dimensional transient model to conduct numerical analysis of the fluid flow and heat transfer in keyhole PAW process, and the volume of fluid (VOF) method was used to track the keyhole boundary [15, 16]. The dynamic evolution of the keyhole shape and its interaction with the weld pool were numerically simulated. With consideration of large depth/width ratio welds produced by keyhole PAW, combined

T. Q. Li · C. S. Wu (✉)
MOE Key Lab for Liquid–Solid Structure Evolution and Materials Processing, and Institute of Materials Joining, Shandong University, Jinan 250061, China
e-mail: wucs@sdu.edu.cn

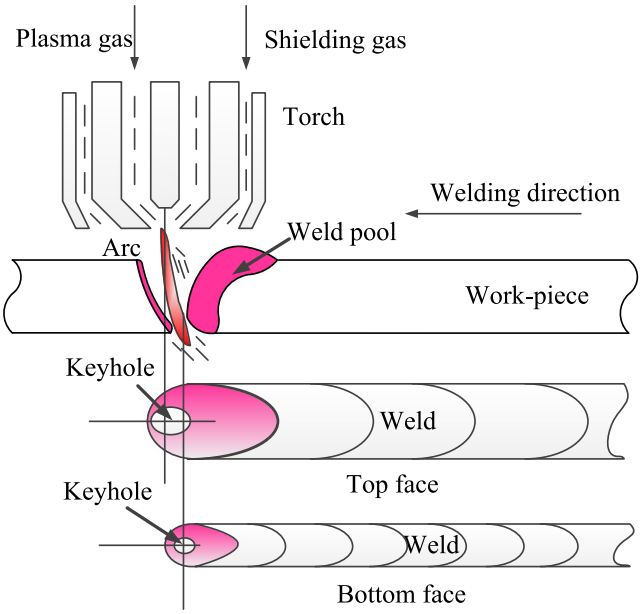

Fig. 1 Schematic of plasma arc welding process

volumetric heat sources, i.e., "double half-ellipsoid plus cylinder" or "double half-ellipsoid plus conic frustum," were used [15, 16]. However, the keyhole effect is just indirectly taken into consideration by adjusting the height of the cylinder or conic frustum according to the variation of keyhole depth. In addition, a constant distribution of the plasma arc pressure was used [15, 16], which means that the arc force acted on the keyhole wall does not vary with the keyhole evolution.

In this study, appropriate distribution modes of both heat flux and arc pressure exerted on the keyhole wall are established. The thermal and mechanical actions from the plasma arc are dynamically adjusted with the variation of keyhole size and shape. As the keyhole evolves from blind status to open status, the curvature of keyhole boundary changes with time, and the distributions of heat intensity and arc pressure along the keyhole wall are correspondingly varied. In this way, three-dimensional fluid flow and heat transfer in the weld pool with a dynamic keyhole is performed, and the prediction results are verified.

2 Mathematical model

Figure 2 shows the three-dimensional geometry domain for numerical simulation. The coordinate origin locates at the top surface of the workpiece, the welding direction is identical to the positive x-axis, and the z-axis is along the thickness of the plate.

2.1 Governing equations

The molten metal in weld pool is taken as viscous and incompressible, and fluid is assumed as laminar. The governing differential equations used to describe heat transfer and fluid flow in the weld pool are given as follows.

Continuity equation

$$\frac{\partial \rho}{\partial t} + \nabla\cdot\left(\rho \vec{v}\right) = 0 \tag{1}$$

where ρ is the density, t is time, and $\vec{v}$ is the vector of the velocity.

Momentum equation

$$\frac{\partial}{\partial t}(\rho u) + \nabla\cdot\left(\rho u \vec{v}\right) = -\frac{\partial p}{\partial x} + \nabla\cdot\nabla(\mu u) + F_x \tag{2}$$

$$\frac{\partial}{\partial t}(\rho v) + \nabla\cdot\left(\rho v \vec{v}\right) = -\frac{\partial p}{\partial y} + \nabla\cdot\nabla(\mu v) + F_y \tag{3}$$

$$\frac{\partial}{\partial t}(\rho w) + \nabla\cdot\left(\rho w \vec{v}\right) = -\frac{\partial p}{\partial z} + \nabla\cdot\nabla(\mu w) + F_z \tag{4}$$

where u, v, and w are the velocity components in x, y, and z directions, respectively; p is the pressure; μ is viscosity; and F_x, F_y, and F_z are the momentum source terms in x, y, and z directions, respectively.

Energy equation

$$\frac{\partial}{\partial t}(\rho H) + \nabla\cdot\left(\vec{v}\rho H\right) = \nabla\cdot(k\nabla T) + S_h \tag{5}$$

where H is the enthalpy of material, k is thermal conductivity, and S_h is the energy source term. H is written as follows.

$$H = h + \Delta H \tag{6}$$

$$h = h_{\mathrm{ref}} + \int_{T_{\mathrm{ref}}}^{T} c_p \mathrm{d}T \tag{7}$$

$$\Delta H = \beta L \tag{8}$$

$$\beta = \begin{cases} 0 & \text{if } T \le T_s \\ \dfrac{T - T_s}{T_l - T_s} & \text{if } T_s < T < T_l \\ 1 & \text{if } T \ge T_l \end{cases} \tag{9}$$

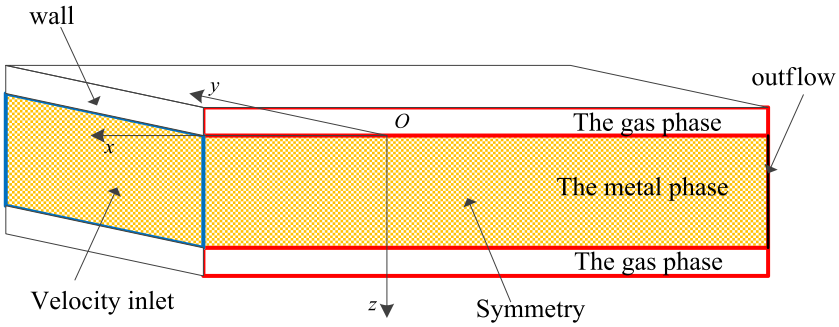

Fig. 2 Geometry model for simulating

where h is sensible enthalpy, ΔH is latent heat, h_{ref} is the reference enthalpy, T_{ref} is the reference temperature, c_p is specific heat at constant pressure, T is the temperature, β is the liquid fraction, L is the heat of fusion, and T_s and T_l are the solidus temperature and the liquid temperature, respectively.

The volume of fluid (VOF) method is used to track the keyhole boundary.

VOF equation

$$\frac{\partial}{\partial t}(\phi\rho_s) + \nabla\cdot\left(\phi\rho_s\vec{v_s}\right) = 0 \tag{10}$$

where ρ_s is the density of the molten metal, v_s is the fluid velocity at the interface, and the function ϕ is defined as follows. If ϕ=0, the cell is full with the plasma arc; if ϕ=1, the cell is full with the molten metal; if 0<ϕ<1, the cell is occupied by both the plasma arc and the molten metal.

The function ϕ is used to determine the normal of the keyhole wall ($\vec{n}$).

$$\vec{n} = \frac{\nabla\phi}{|\nabla\phi|} = \frac{\phi_x\vec{i} + \phi_y\vec{j} + \phi_x\vec{k}}{\sqrt{\phi_x^2+\phi_y^2+\phi_z^2}} = n_x\vec{i} + n_y\vec{j} + n_z\vec{k} \tag{11}$$

2.2 Source terms at the physical boundary

The heat flux and pressure from the plasma arc are acted on the keyhole wall, i.e., the physical boundary between the plasma jet and the molten metal. Special source terms are set to deal with this physical boundary.

In energy equation Eq. (2), the source term S_h is used to describe the heat transfer from the plasma arc to the workpiece and the heat loss from the workpiece to the ambient atmosphere. The source term S_h is just available at the physical boundary, as schematically shown in Fig. 3. To limit this source term within the grid nodes along the physical boundary, following functions are defined as follows,

$$\delta_1(|\nabla\phi|) = \begin{cases} 1 & \text{if } \phi\geq\varepsilon_1 \text{ and } |\nabla\phi|\geq\varepsilon_2 \text{ and } \phi_z\geq\varepsilon_3 \\ 0 & \text{else} \end{cases} \tag{12}$$

$$\delta_2(|\nabla\phi|) = \begin{cases} 1 & \text{if } \phi\geq\varepsilon_1 \text{ and } |\nabla\phi|\geq\varepsilon_2 \\ 0 & \text{else} \end{cases} \tag{13}$$

where ε_1, ε_2, and ε_3 are small numbers corresponding to the position and curvature of the nodes in the grid system. When $\delta_1(|\nabla\phi|)$=1, the nodes locate on the keyhole wall. When $\delta_2(|\nabla\phi|)$=1, the nodes locate on the physical boundary including top and bottom surfaces of the molten pool. With the help of Eqs. (12) and (13), the source term S_h is written as

$$S_h = \delta_1(|\nabla\phi|)q(x,y)/z_{\text{foot}} - \delta_2(|\nabla\phi|)\alpha_T[T(x,y,z)-T_0]/z_{\text{foot}} \tag{14}$$

where $q(x,y)$ is the heat flux from the plasma arc, z_{foot} is the grid size in z direction, α_T is combined heat loss coefficient, and T_0 is the ambient temperature.

Similarly, the plasma arc pressure just acts on the keyhole wall, while the surface tension acts on all molten metal surfaces. For the momentum equations Eqs. (2), (3), and (4), the source terms contains the body force and the surface force. Here, the body forces, i.e., the electromagnetic force, the resistance force due to the reduced porosity in the mushy zone and the gravity, can be directly added to the source term of the momentum equation. However, the surface forces, i.e., the plasma arc pressure and the surface tension, have to be dealt with by employing the functions $\delta_1(|\nabla\phi|)$ and $\delta_2(|\nabla\phi|)$ so that they are limited to the physical boundary.

$$F_x = Fe_x + Fm_x + \delta_2(|\nabla\phi|)Fst_x/x_{\text{foot}} + \delta_1(|\nabla\phi|)P_x/x_{\text{foot}} \tag{15}$$

$$F_y = Fe_y + Fm_y + \delta_2(|\nabla\phi|)Fst_y/y_{\text{foot}} + \delta_1(|\nabla\phi|)P_y/y_{\text{foot}} \tag{16}$$

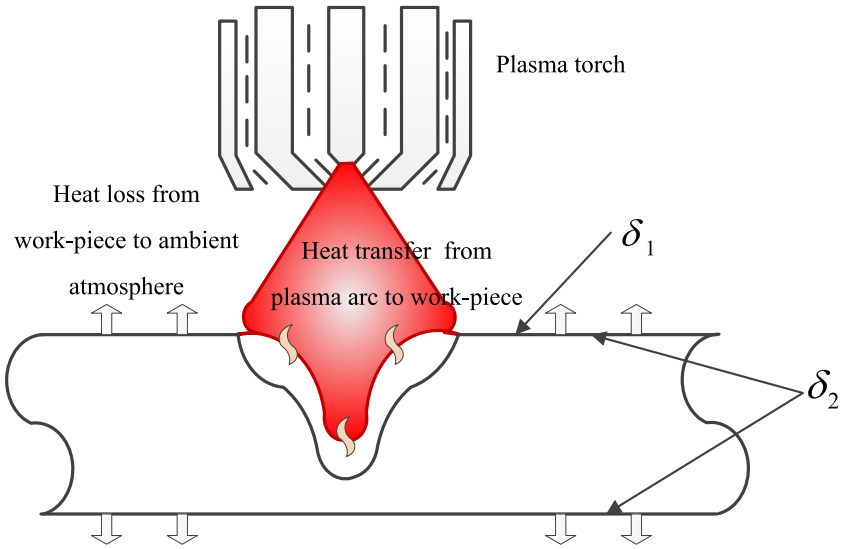

Fig. 3 The description of heat transfer on the physical boundary

$$F_z = Fe_z + Fm_z + \rho g + \delta_2(|\nabla\phi|)Fst_z/z_{\text{foot}} + \delta_1(|\nabla\phi|)P_z/z_{\text{foot}} \tag{17}$$

where (Fe_x,Fe_y,Fe_z) are the electromagnetic force components, (Fm_x,Fm_y,Fm_z) are the components of the resistance force due to reduced porosity in mushy zone, (Fst_x,Fst_y,Fst_z) are the surface tension components, (P_x,P_y,P_z) are the plasma arc force components, and $(x_{\text{foot}},y_{\text{foot}},z_{\text{foot}})$ are the grid sizes in x,y,z directions, respectively.

The component Fe_x, Fe_y, and Fe_z can be expressed as follows,

$$Fe_x = -\frac{\mu_0 I^2}{4\pi^2\sigma_j^2 r^2}\exp\left(-\frac{r^2}{2\sigma_j^2}\right)\left[1-\exp\left(-\frac{r^2}{2\sigma_j^2}\right)\right]\left(1-\frac{z}{ZL}\right)^2 x \tag{18}$$

$$Fe_y = -\frac{\mu_0 I^2}{4\pi^2\sigma_j^2 r^2}\exp\left(-\frac{r^2}{2\sigma_j^2}\right)\left[1-\exp\left(-\frac{r^2}{2\sigma_j^2}\right)\right]\left(1-\frac{z}{ZL}\right)^2 y \tag{19}$$

$$Fe_z = \frac{\mu_0 I^2}{4\pi^2 ZLr^2}\left[1-\exp\left(-\frac{r^2}{2\sigma_j^2}\right)\right]^2\left(1-\frac{z}{ZL}\right) \tag{20}$$

where μ_0 is the space permeability, I is the welding current, σ_j is the distribution parameter of the current density, and ZL is the thickness of the workpiece.

The component Fm_x Fm_y and Fm_z can be expressed as follows,

$$Fm_x = \frac{(1-\beta)^2}{(\beta^3+\xi_1)}A_{\text{mush}}[u-(-u_w)] \tag{21}$$

$$Fm_y = \frac{(1-\beta)^2}{(\beta^3+\xi_1)}A_{\text{mush}}v \tag{22}$$

$$Fm_z = \frac{(1-\beta)^2}{(\beta^3+\xi_1)}A_{\text{mush}}w \tag{23}$$

where ξ_1 is a small positive number to prevent the division by zero, A_{mush} is the mushy zone constant, and u_w is the welding speed.

The component Fst_x, Fst_y, and Fst_z can be expressed as follows,

$$Fst_x = \gamma\frac{\rho\kappa n_x}{{}^1/_2\left(\rho_f+\rho_s\right)} \tag{24}$$

$$Fst_y = \gamma\frac{\rho\kappa n_y}{{}^1/_2\left(\rho_f+\rho_s\right)} \tag{25}$$

$$Fst_z = \gamma\frac{\rho\kappa n_z}{{}^1/_2\left(\rho_f+\rho_s\right)} \tag{26}$$

$$\kappa = \nabla\cdot\vec{n} \tag{27}$$

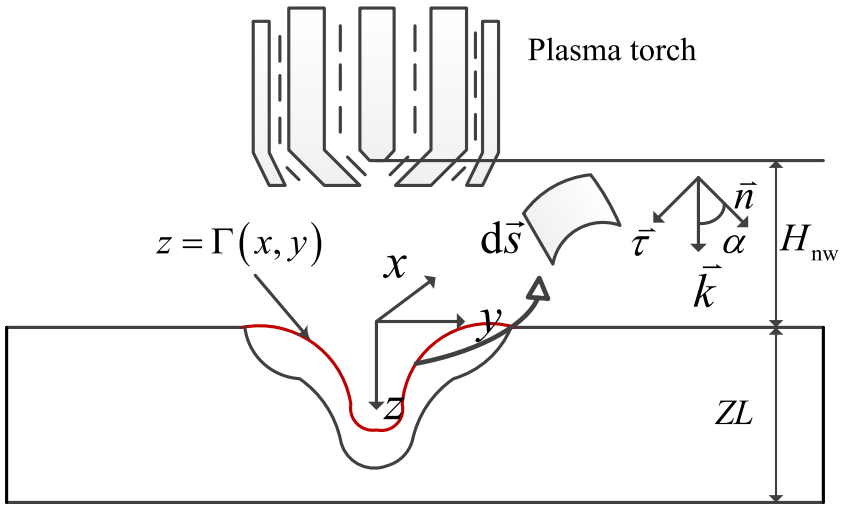

Fig. 4 Visual sketch of variable definition

where γ is the surface tension, κ is the curvature, ρ_f is the density of the gas phase, and ρ_s is the density of the molten metal, respectively, and $^1/_2\left(\rho_f+\rho_s\right)$ means the average density in the cell.

When the plasma jet impinges on the keyhole wall, the action force on the keyhole wall can be decomposed into the normal force and the tangential force on the keyhole wall, shown as Fig. 4. In this model, the tangential force is ignored. The plasma arc pressure components (P_x, P_y, P_z) are written as

$$P_x = P(x,y)\cos\alpha\cdot n_x \tag{28}$$

$$P_y = P(x,y)\cos\alpha\cdot n_y \tag{29}$$

$$P_z = P(x,y)\cos\alpha\cdot n_z \tag{30}$$

$$\cos\alpha = \vec{n}\cdot\vec{k} \tag{31}$$

where α is the angle between the normal direction and vertical direction, as shown in Fig. 4.

2.3 Heat flux at the curved keyhole wall

As shown in Fig. 4, the keyhole boundary is defined by the shape function $\Gamma(x,y)$. At the very starting moment, the workpiece surface is flat, and $z=\Gamma(x,y)=0$. Then, the weld pool surface is depressed, blind keyhole is formed, and the curved boundary of keyhole is described by $z=\Gamma(x,y)$. Due to the keyhole establishment, thermal energy from the plasma arc is deposited on the curved keyhole wall. As keyhole develops from blind status to open status, the curvature of the keyhole wall gets larger, so that the thermal deposition condition changes a lot. The heat flux on the keyhole wall should be dependent on the shape and size of keyhole. To take account for this phenomenon, a modified distribution mode of thermal energy on the keyhole wall is proposed.

$$q(x,y) = \left[1-\frac{\Gamma(x,y)}{ZL+H_{nw}}\right]^2 q_{max}\exp\left[-\frac{3(x^2+y^2)}{r_q^2}\right] \tag{32}$$

$$\eta I U_a = \int_{\Gamma(x,y)} q(x,y)\,\mathrm{d}\vec{s}\cdot\vec{k} \tag{33}$$

where ZL is the thickness of the workpiece, H_{nw} is the distance from nozzle to workpiece, q_{max} is the maximum heat intensity at the central axis when anode surface is flat, r_q is the

Table 1 Welding parameters and material properties

Parameters	Value
Welding current (A)	140.0
Arc voltage (V)	22.0
Distance from electrode to workpiece (m)	0.005
Nozzle diameter (m)	0.0028
Plasma gas flow rate (m^3/s)	5×10^{-5}
Shielding gas flow rate (m^3/s)	3.333×10^{-4}
Workpiece thickness (m)	0.006
Welding speed (m/s)	0.002
Thermal conductivity of 304 stainless steel (W/K m)	28.4
Density of 304 stainless steel (kg/m^3)	6800
Viscosity (liquid) of 304 stainless steel (Pa s)	0.005
Specific heat (J/kg K)	760
Liquid temperature (K)	1727
Solidus temperature (K)	1672

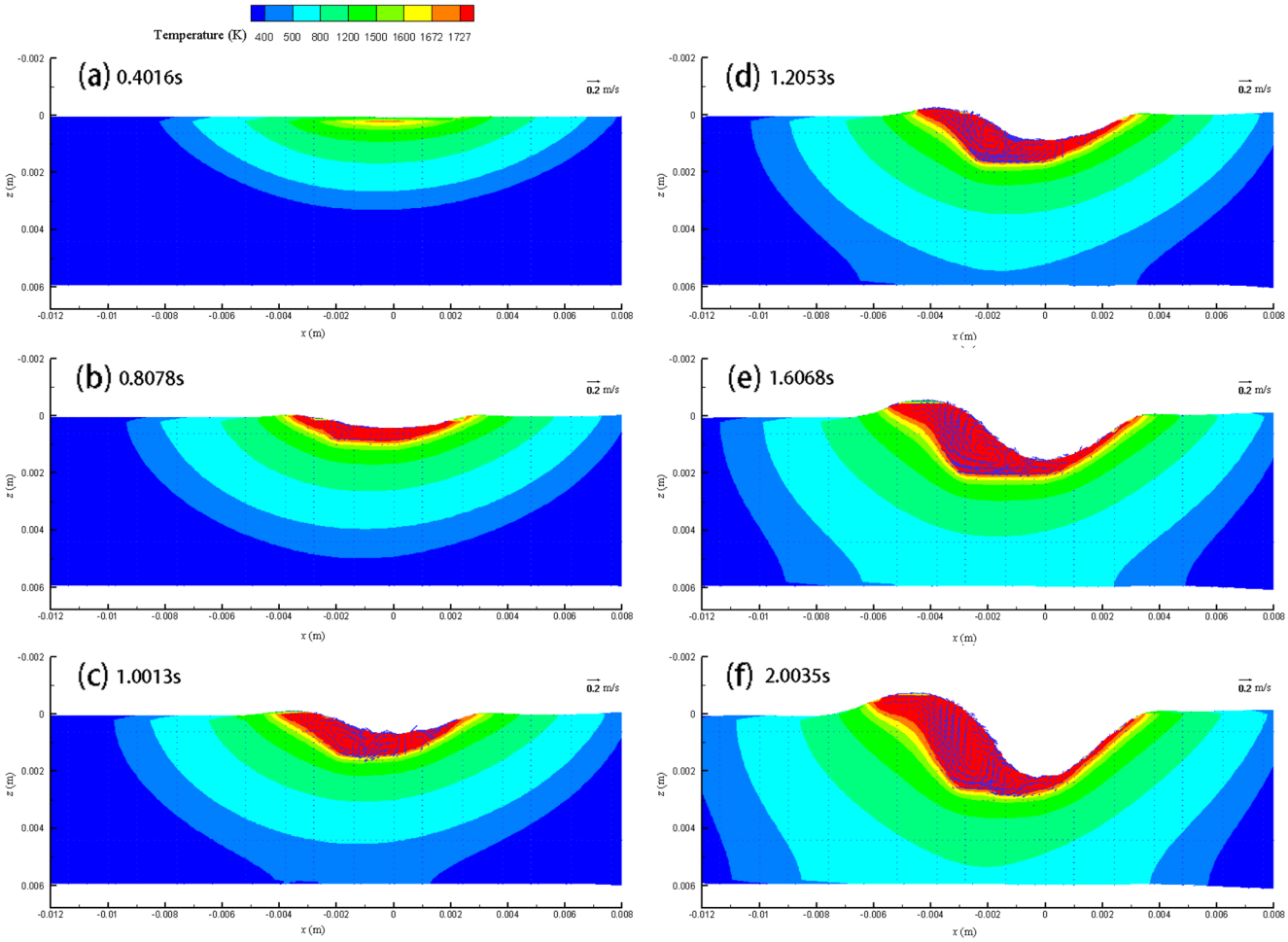

Fig. 5 The evolution of temperature field, fluid flow in the weld pool, and keyhole surface over time

distribution parameter when anode surface is flat, η is the arc power efficiency, I is the welding current, U_a is the arc voltage, $\mathrm{d}\vec{s}$ is the small area element, and $\vec{k}$ is the unit vector from electrode to workpiece along z direction.

2.4 Arc pressure at the curved keyhole wall

Similarly, the distribution mode of plasma arc pressure varies as the weld pool surface is depressed. When the keyhole boundary gets curved, the distance from the nozzle to a certain point on the keyhole wall is increased. This causes some loss of momentum of plasma jet, so that the arc pressure on the same point is lowered. When open keyhole is established, the efflux plasma exits from the keyhole channel, and the corresponding part of the plasma pressure disappears. To consider this fact, the arc pressure at the curved keyhole wall is expressed as follows.

$$P(x,y)=\left(1-\frac{\Gamma(x,y)}{ZL+H_{\mathrm{nw}}}\right)^2 C_f\frac{\mu_0 I^2}{4\pi^2 r_p^2}\exp\left(-3\frac{x^2+y^2}{r_p^2}\right) \quad (34)$$

$$C_f=\frac{3r_{\mathrm{noz}}^2\rho_{\mathrm{Ar}}\sqrt{\dfrac{2\eta_v IUQ_{\mathrm{Plas}}}{\rho_{\mathrm{Ar}}S_{\mathrm{noz}}^2}+\dfrac{Q_{\mathrm{Plas}}^4}{S_{\mathrm{noz}}^4}}}{A_I} \quad (35)$$

where C_f is the interrelated factor with welding parameters [17], μ_0 is the space permeability, r_P is the radius of plasma arc pressure impacting on the workpiece, r_{noz} is the nozzle radius, ρ_{Ar} is the gas density, η_v is the conversion coefficient, Q_{plas} is the plasma gas flow rate, S_{noz} is the area of the nozzle, and A_I is an adjusting constant.

3 Result and discussion

The governing equations and their boundary conditions are transformed into finite difference equations by employing a finite-volume method. Non-uniform grid system is used to discretize the calculation domain. Finer grids are chosen in the region of weld pool to deal with higher temperature gradient

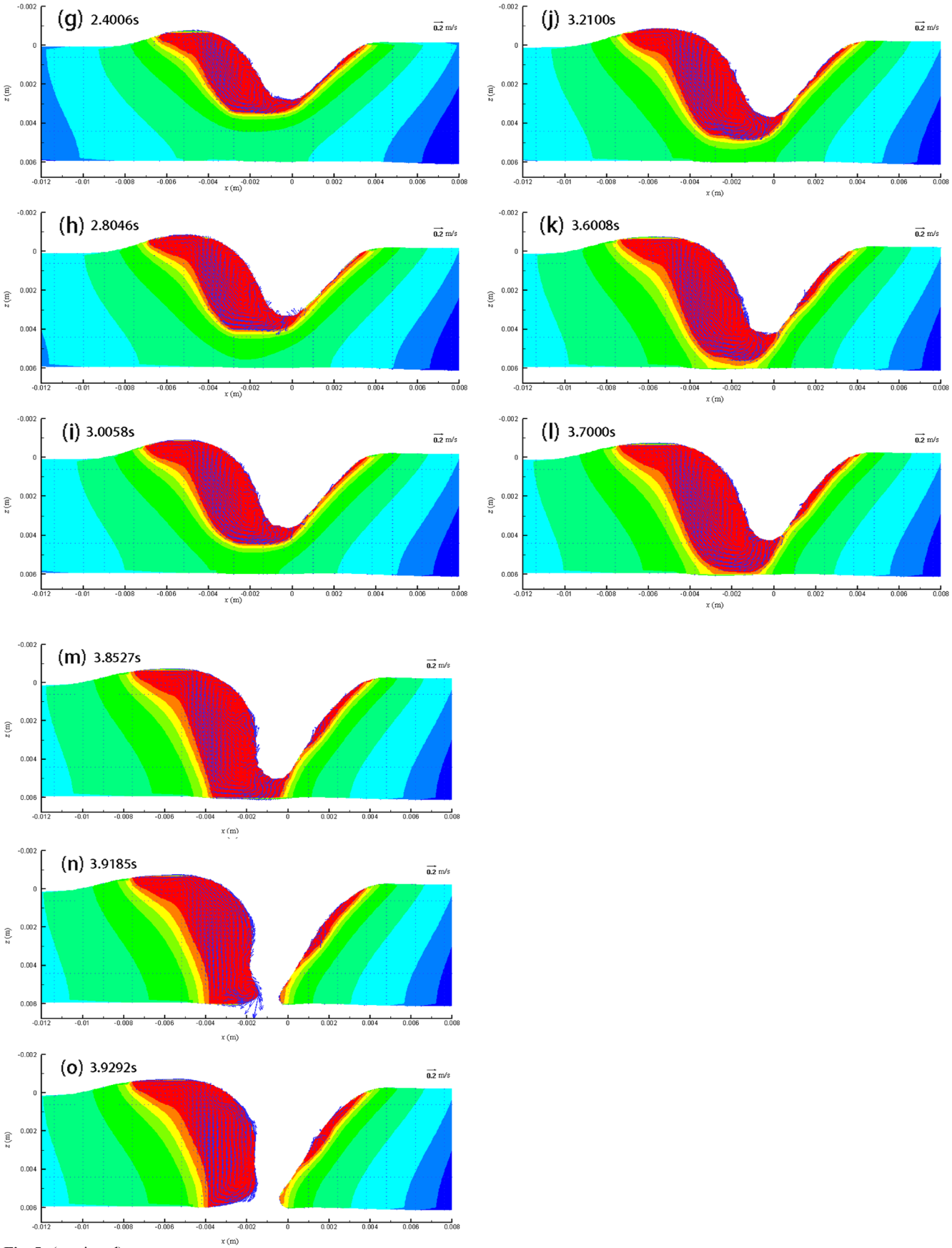

Fig. 5 (continued)

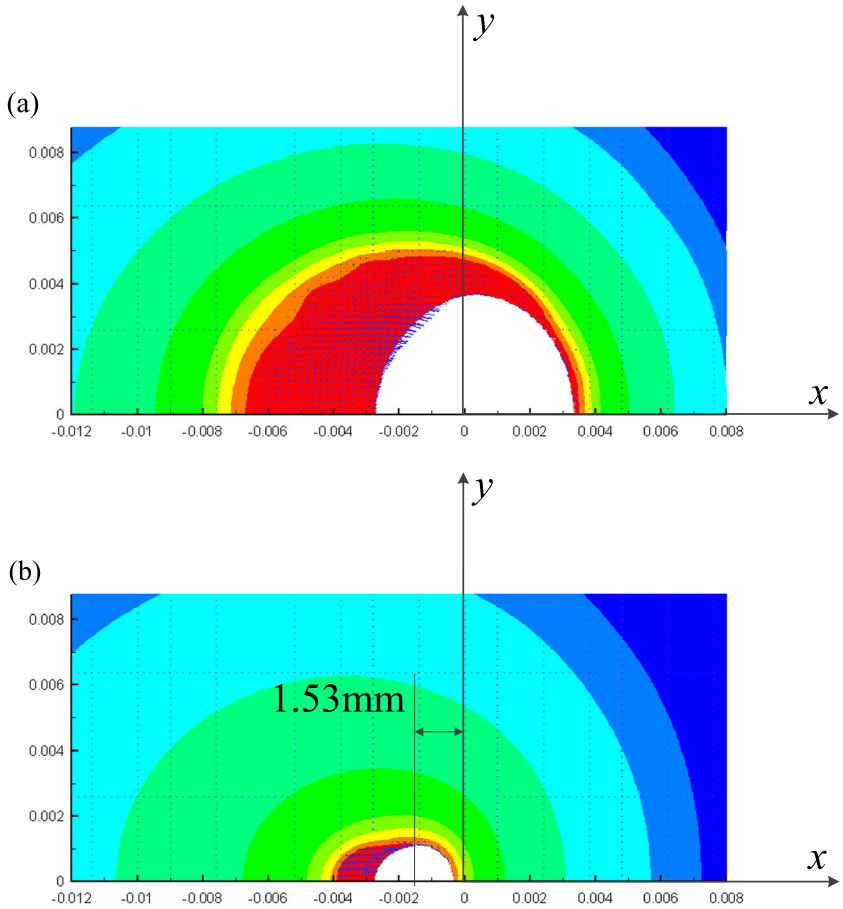

Fig. 6 Temperature distribution and keyhole shape on time 3.9292 s: **a** top surface and **b** bottom surface

and fluid convection effectively. The commercial code ANSYS Fluent 14.5 is used to perform the numerical analysis. The plate of 304 stainless steel with thickness 6 mm is taken as the workpiece welded by plasma arc welding. As shown in Fig. 2, the calculation domain includes the steel plate and the surrounding air layers. The welding speed is 120 mm/min. For the velocity inlet, the steel plate moves along with the *x*-axis at the speed of −0.002 m/s. The *xoz* plane is the symmetry boundary. Wall condition is taken for other boundaries.

Both convection and radiation heat loss from the workpiece surfaces are considered. The heat loss coefficient is 40 W/(m^2 k), and the emissivity is 0.1. The other material properties are shown in Table 1. For simplification, the specific heat and thermal conductivity are taken as independent of temperature at the first step. The welding parameters taken in the simulation are also written in Table 1. The surface tension is changing with temperature [18].

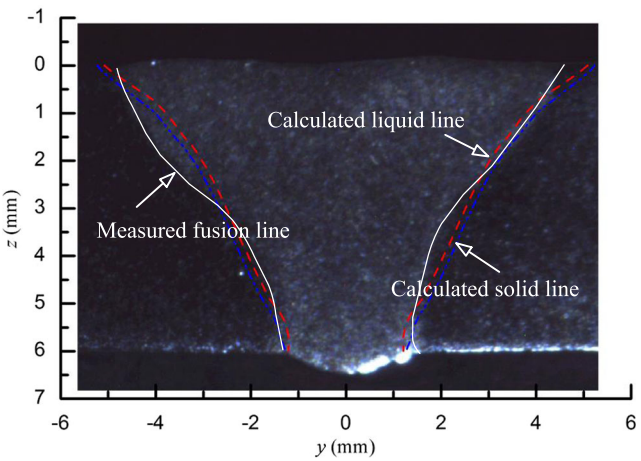

Fig. 7 Comparison of the calculated fusion line with the experimental one

$$\gamma = \gamma_m - A(T - T_m) - RT\Gamma_s \ln\left[1 + k_l a_s \exp\left(-\Delta H^0/RT\right)\right] \quad (36)$$

$$\frac{\partial \gamma}{\partial T} = -A - R\Gamma_s \ln\left(1 + K_{\text{seg}} a_s\right) - \frac{K_{\text{seg}} a_s \Delta H^0 \Gamma_s}{T\left(1 + K_{\text{seg}} a_s\right)} \quad (37)$$

$$K_{\text{seg}} = k_l \exp\left(-\Delta H^0/RT\right) \quad (38)$$

where γ_m, A, Γ_s, a_s, ΔH^0, and k_l are the surface tension of pure iron at melting point, temperature coefficient of pure

iron, saturation parameter, thermodynamic activity of sulfur, standard heat of absorption, and entropy factor, respectively.

Figure 5 shows the transient evolution of the keyhole shape, temperature field, and fluid flow in the weld pool at longitudinal cross-section. Different colors represent the temperature scale, and the arrows in the pictures demonstrate the fluid velocity vector inside the weld pool. When the plasma arc deposits both thermal energy and pressure on the workpiece, the molten pool is formed, and its volume expands quickly, as shown in Fig. 5a–c. Then, the plasma arc pressure causes a depression of the weld pool surface, and a blind keyhole (cavity) starts to form, as demonstrated in Fig. 5d–f. The blind keyhole is unsymmetrical with respect to the torch axis (x=0). Lots of molten metal accumulates at the rear part of weld pool, and the molten metal layer at the front part of weld pool is much thinner than that at the rear part of weld pool. As time goes on, the sizes of both weld pool and keyhole increase, the liquid layer at the front part of weld pool becomes thinner and thinner, and it even contains only the mushy zone at some parts, as shown in Fig. 5g–k. Then, the workpiece is fully penetrated, i.e., the bottom surface is melted, as illustrated in Fig. 5l–m. At a certain moment, a complete keyhole (open keyhole) is established, as shown in Fig. 5*n*. When this keyhole penetrates entirely through the thickness of the workpiece, front keyhole wall almost closes to the melt front. Generally, the fluid flow field becomes stronger with expanding of weld pool. It can be seen from Fig. 5 that a clear clockwise flow circle is found in the rear part of the weld pool. Firstly, the molten metal flows downwards along the free surface under the action of plasma arc pressure, and then it flows upwards along the rear edge of weld pool.

With observing Fig. 5, one can find another phenomenon, i.e., the keyhole channel is curved backward with respect to the torch axis. The experiments once shown that the keyhole exit is displaced in the direction opposite to the welding direction since the keyhole channel is curved backward [19]. The deviation of the keyhole exit from the torch axis is due to the relative motion between the torch and the workpiece. Because this model employs the dynamic varied distribution of both heat flux and pressure from the plasma arc, which is dependent on the curvature of keyhole wall, thus the backward curved keyhole channel is numerically simulated.

PAW experiments were made to verify the calculated results. The test conditions are shown in Table 1. When an open keyhole is formed, the efflux plasma exited form the keyhole channel will produce an electrical signal [2]. Detecting this signal will give the open keyhole establishment time. The CCD camera was also used to capture the images of keyhole from backside of the workpiece [19], and the sequential images will give the open keyhole establishment time. The measured establishment time of open keyhole is 4.68 s, while the calculated value of this time is 3.9185 s. The measured displacement of keyhole exit at backside is 0.54 mm, while the predicted data is 1.53 mm as shown in Figs. 6 and 7 is the comparison between the calculated and measured fusion line. The experimentally measured and numerical simulated results match with each basically, but the prediction accuracy of the model needs further improvement.

4 Summery and conclusion

A transient and three-dimensional model of PAW process is developed with considering the dynamic variation of both heat flux and arc pressure distribution on the keyhole wall. As keyhole evolves from blind status to open status, the deposition modes of heat and pressure from the plasma arc on keyhole boundary are adaptively adjusted at each time step, and the heat transfer and fluid flow in weld pool are numerically simulated. With the keyhole geometry-dependent heat source and arc pressure, the experimentally observed phenomena, i.e., the backward curved keyhole channel and the very thin layer of molten metal at the front edge of weld pool, are first demonstrated with numerical simulation. Keyhole PAW experiments are conducted to verify the model. The predicted results including the establishment time of open keyhole and displacement of keyhole exit and fusion line generally match with the experimentally measured ones under the used test conditions.

Acknowledgments The authors wish to thank the National Natural Science Foundation of China (Grant No. 50936003) for the support of this research.

References

1. Zhang YM, Zhang SB (1999) Observation of the keyhole during plasma arc welding. Weld J 75(2):53–59
2. Wu CS, Wang L, Ren WJ, Zhang XY (2014) Plasma arc welding: process, sensing, control and modeling. J Manuf Proc 16(1):74–85
3. Meng C, Lu FG, Cui HC, Tang XH (2013) Research on formation and stability of keyhole in stationary laser welding on aluminum MMCs reinforced with particles. Int J Adv Manuf Technol 67: 2917–2925
4. Cho WI, Na SJ, Thomy C, Vollertsen F (2012) Numerical simulation of molten pool dynamics in high power disk laser welding. J Mater Process Technol 212:262–275
5. Li X, Lu F, Cui H, Tang X, Wu Y (2014) Numerical modeling on the formation process of keyhole-induced porosity for laser welding steel with T-joint. Int J Adv Manuf Technol 72:241–254
6. Martikainen JK, Moisio TJI (1993) Investigation of the effect of welding parameters on weld quality of plasma arc keyhole welding of structural steels. Weld J 2(7):329–340
7. Fortain JM (2008) Plasma welding evolution & challenges. International Institute of Welding Document XII 1948(08):1–11
8. Wu CS, Hu QX, Gao JQ (2009) An adaptive heat source model for finite-element analysis of keyhole plasma arc welding. Comput Mater Sci 46:167–172

9. Daha MA, Nassef GA, Abdallah IA (2012) Numerical modeling of heat transfer and fluid flow in keyhole plasma arc welding of dissimilar steel joints. Int J Eng Sci Tech 4(2):506–518
10. Keanini RG, Rubinsky B (1993) Three-dimensional simulation of the plasma arc welding process. Int J Heat Mass Transfer 36(13):3283–3298
11. Nehad AK (1995) Enthalpy technique for solution of stefan problems: application to the keyhole plasma arc welding process involving moving heat source. Int Comm Heat Mass Tran 22(6):779–790
12. Fan HG, Kovacevic R (1999) Keyhole formation and collapse in plasma arc welding. J Phys D Appl Phys 32:2902–2909
13. Li TQ, Wu CS, Feng YH, Zheng LC (2012) Modeling of the thermal fluid flow and keyhole shape in stationary plasma arc welding. Int J Heat Fluid Fl 34:117–125
14. Li Y, Feng YH, Zhang XX, Wu CS (2014) Energy propagation in plasma arc welding with keyhole tracking. Energy 64:1044–1056
15. Zhang T, Wu CS, Feng YH (2011) Numerical analysis of heat transfer and fluid flow in keyhole plasma arc welding. Numer Heat Tr A-Appl 60(8):685–698
16. Wu CS, Zhang T, Feng YH (2013) Numerical analysis of the heat transfer and fluid flow in a weld pool with a dynamic keyhole. Int J Heat Fluid Fl 40:186–197
17. Li TQ, Wu CS (2014) An analytic formula describing the plasma arc pressure distribution. China Welding 23(2):7–11
18. Sahoo P, Debroy T, McNallan M (1988) Surface tension of binary metal—surface active solute systems under conditions relevant to welding metallurgy. Metal Mater Trans B 19(3):483–491
19. Liu Z, Wu CS, Chen M (2014) Experimental sensing of the keyhole exit deviation from the torch axis in plasma arc welding. Int J Adv Manuf Technol 71:1209–1219